THE ASTROPHYSICAL JOURNAL, 1006:62 (12pp), 2026 July 20 https://doi.org/10.3847/1538-4357/ae815a

Density Increases in the Cometary Plasma Environment and Their Relation to Magnetosheath Jets

Charlotte Goetz[1], Ruben Doyle-Morgan[1], Herbert Gunell[2], Eva Krämer[2], Tomas Karlsson[3], Anja Möslinger[2], Cyril Simon-Wedlund[4], and Martin Volwerk[5]
[1] Northumbria University, Newcastle, UK; charlotte.goetz@northumbria.ac.uk
[2] Umeå University, Umeå, Sweden
[3] KTH, Stockholm, Sweden
[4] Institute of Physics, University of Graz, Graz, Austria
[5] IWF, Graz, Austria
Received 2026 April 27; revised 2026 May 28; accepted 2026 June 9; published 2026 July 15

Abstract

In the cometary plasma environment, the solar wind interacts with the expanding coma of heavy cometary ions. At high gas production rates, it can have plasma environment characteristics similar to the environment of Mars, with a bow shock and a cometosheath. Magnetosheath jets are transient enhancements in the dynamic pressure of the magnetosheath plasma. They can be generated at a disturbed bow shock surface and have been confirmed at Mars, Earth, and possibly Jupiter and Mercury. We have adapted commonly used methods to find magnetosheath jets to the Rosetta data at 67P/Churyumov–Gerasimenko and find candidate events throughout the postperihelion mission. We show that the identified density enhancements have similarities to magnetosheath jets. The events are of typical duration and density enhancement, and occur at a time when the bow shock is thought to be close to the spacecraft. We found a cometary ion velocity enhancement, although no conclusion on the solar wind velocity can be reached due to lack of data. These jet-like features are embedded in the heavy-ion population. We hypothesize that jets are formed in the solar wind ion population in the cometosheath, and then, as the two plasmas interact, are transferred to the cometary ion population. While we cannot rule out other phenomena that could cause these jet-like enhancements, they bear a remarkable resemblance to magnetosheath jets at Mars and Earth. If they are indeed jets, then this is the first time jets have been shown to exist in a plasma environment dominated by heavy ions.

Unified Astronomy Thesaurus concepts: Solar wind (1534); Comets (280); Magnetosheath (2381); Space plasmas (1544)

1. Introduction

As comets near the Sun, the ices on the surface sublimate and create a neutral gas cloud consisting mostly of water around the comet (M. Läuter et al. 2020). Photoionization, electron-impact ionization, and solar wind charge-exchange reactions lead to the creation of heavy ions of cometary origin (mostly water) and photoelectrons. As the ions are born at a neutral escape velocity speed of <1 km s^{-1}, they constitute an obstacle to the solar wind and its interplanetary magnetic field (IMF). The interaction between the cometary and solar wind plasma is complex and strongly depends on the outgassing rate of the comet. For this study, we will only focus on what have been termed the "high-activity" and "intermediate-activity" stages (C. Goetz et al. 2022). At these stages, cometary ions start to be created from neutrals tens of thousands of kilometers upstream of the nucleus, where they are accelerated by the interaction with the solar wind and its convective electric field. As energy and momentum are transferred from the solar wind to the cometary ions, the bulk flow velocity of the solar wind decreases gradually as it approaches the comet until a critical mass threshold is reached. At this point a bow shock forms (C. Koenders et al. 2013; H. Gunell et al. 2018; N. J. T. Edberg et al. 2024). Downstream of the bow shock, the solar wind ions are gradually deflected away from the Sun-comet line while exchanging momentum and energy with the heavy cometary ions that are flowing anti-sunward. A solar wind ion cavity forms, within which no solar wind ions are detected, and cometary ions carry all of the flow momentum (E. Behar et al. 2017; H. N. Williamson et al. 2020). The region behind the bow shock and, to some extent, within the solar wind ion cavity is analogous to a planetary magnetosheath in the sense that it is filled with roughly anti-sunward flowing plasma, with flow velocities smaller than the solar wind flow velocity. It is therefore often called the "cometosheath."

Magnetosheath jets are transient dynamic pressure enhancements that are thought to predominantly originate at quasi-parallel bow shocks and propagate through the magnetosheath at planets such as Earth and Mars (F. Plaschke et al. 2018a; E. Krämer et al. 2025). In identification methods, jets have generally been defined as enhancements in the dynamic pressure (sometimes only calculated from the speed in the antisolar direction) that exceed background values or solar wind values and are unrelated to structures in the solar wind (Z. Němeček et al. 1998).

F. Plaschke et al. (2018a) summarize statistical studies of the properties of jets at Earth. Generally, jets are found to be 0.1–2.8 Earth radii in size, with most jets exhibiting an increase in the anti-sunward plasma velocity. The ion temperature is almost isotropic within the jet, and the magnetic field can decrease or increase within it. All jets exhibit, by definition, an increase in dynamic pressure, but the contribution to this enhancement by the velocity and density is variable. For example, at Earth, more jets are driven by a velocity increase (H. Hietala et al. 2009), although some studies find that jets behind the quasi-parallel bow shock often have noticeable density increases (S. Raptis et al. 2020). T. Karlsson et al. (2015) found that density-driven structures occur often, and these have been called “plasmoids” by other authors. The size of jets is highly variable, and the choice of selection criteria influences the estimate of jet size. Considering the observation bias, the median perpendicular (to the flow) size is $\sim$800 km and the median parallel size is $\sim$1000 km (F. Plaschke et al. 2020).

Magnetosheath jets at Earth are generally associated with the region behind a quasi-parallel bow shock (F. Plaschke et al. 2013; E. Krämer et al. 2025). Jet occurrence decreases steadily with increasing angle between the IMF and the bow shock normal (S. Raptis et al. 2020). Most studies find that jets more often occur closer to the bow shock, but they can be found throughout the magnetosheath. Jets mostly occur under stable solar wind conditions, implying that a stable foreshock region is conducive to jet formation. There is no distinct periodicity to the occurrence of jets in any study.

The key processes leading to the formation of jets seem to be related to nonlinear structures in the foreshock (J. Suni et al. 2021) or ripples of the bow shock surface itself (H. Hietala et al. 2009). Simply put, bow shock ripples allow small parcels of solar wind plasma to traverse the bow shock without being decelerated, in contrast to the plasma around them. This parcel then becomes a high dynamic pressure structure as it is compressed by the surrounding bow shock morphology (S. Raptis et al. 2022). Solar wind discontinuities can also cause jet formation at both the quasi-parallel and quasi-perpendicular bow shock as shown in simulations (J. Suni et al. 2025; J. Guo et al. 2026) and data (M. O. Archer et al. 2012).

Jets then propagate through the magnetosheath, where they modify the surrounding plasma, bend the magnetic field (F. Plaschke et al. 2020), and some even form a local shock front that precedes the bulk of the jet (F. Plaschke et al. 2013). There is some evidence that jets are decelerated as they traverse the magnetosheath (T. Karlsson et al. 2015). Lastly, jets interact with the magnetopause, where they can in turn cause local ripples at the boundary (Z. Němeček et al. 2023) and contribute to substorm onset (K. Nykyri et al. 2019) and aurora (B. Wang et al. 2018). The geoeffectiveness of jets is an object of current study (E. Krämer et al. 2025).

While jets have been mostly studied at Earth due to the availability of excellent multipoint measurements, they have also been detected in the magnetosheaths of other solar system bodies. In the absence of reliable velocity data, magnetic field data can be used to infer the presence of jets. T. Karlsson et al. (2016) used MESSENGER magnetic field data to search for potential jet-like events in the magnetosheath at Mercury. While they could not provide unambiguous proof that the identified structures are indeed jets, they share some characteristics in the magnetic field with jets at Earth. However, the events identified as possible jets could not be related to the quasi-parallel bow shock, casting doubt on the hypothesis that these events are jets. While simulations have also suggested the presence of jets at Mercury (J. Guo et al. 2025), new data from the Bepi-Colombo mission may confirm or deny the presence of jets in the Hermean environment. There is also some evidence that jets exist in the magnetosheath at Jupiter (Y. Zhou et al. 2024); however, measurements are limited to three events found during the Voyager 2 flyby.

H. Gunell et al. (2023) showed for the first time that jets were present in the magnetosheath of Mars. They presented three jet events, two in 2017 January and one in 2020 June. The duration of the jets was found to be 32–60 s, and they were found behind the quasi-perpendicular bow shock. The scale size of the jet was estimated to be 4000–18,000 km; this was larger than the distance between the bow shock and the magnetopause, indicating that jets fill the entire magnetosheath, similar to magnetic holes at comets (F. Plaschke et al. 2018b). One jet did not show any speed enhancement, which was attributed to its location further downstream in the magnetosheath, closer to the induced magnetosphere boundary.

T. Mohammed-Amin et al. (2025) used MAVEN data to identify jets at Mars for a statistical study. They found 82,645 events within the magnetosheath over a 10 yr period from 2014 to 2024. Jet events were found to be dominated by density-driven enhancements, with an average duration of 7 s. They were found to preferentially occur near the bow shock flanks. The velocity within the jet indicates that there is a more significant deflection in the jet than in the surrounding magnetosheath; however, they all still clearly move in the antisolar direction. The median scale size of the jets, calculated from the time and velocity of the plasma, was found to be 0.67 R_M, or 11 proton gyroradii. This makes them smaller than those found at Earth in absolute size, but larger than those at Earth compared to the respective magnetosheath size. Finally, T. Mohammed-Amin et al. (2025) theorize that the increased wave activity in the Martian foreshock due to the upstream ion pickup makes Martian jets less dependent on being formed at the quasi-parallel bow shock. Instead, even the quasi-perpendicular bow shock is more disturbed than at Earth and can therefore be susceptible to jets.

Since Mars is similar to the cometary environment in the sense that there is no global magnetic field at either and instead the solar wind is interacting with an ionosphere, it stands to reason that jets could also exist at comets. The cometary bow shock is highly disturbed by the ion pickup processes upstream of it, and is therefore similar to a quasi-parallel shock. Instabilities generated through pickup processes such as the ion-ion instability contribute to the shock surface degradation and lead to waves and ripples along the surface (F. M. Neubauer et al. 1990). However, due to the multi-ion nature of the plasma, an additional dimension is added: jets may not only occur in the slowed solar wind within the magnetosheath but also in the cometary ion population at a comet. It has been shown that large-scale magnetic field structures such as magnetic holes can survive the transition from solar wind-dominated to cometary ion-dominated plasma (F. Plaschke et al. 2018b), which raises the question as to whether this could also happen to increased density structures like jets.

Jets could be an important contributor to the momentum and energy balance in the cometary environment and link bow shock processes to the plasma in the inner coma. The aim of this paper is to investigate whether jet-like features do indeed exist in the cometary environment at comet 67P/Churyumov–Gerasimenko and whether their properties are similar to magnetosheath jets found at other solar system objects.

2. Methodology

2.1. Instrumentation

We use data provided by the instruments onboard ESA's Rosetta spacecraft (K.-H. Glassmeier et al. 2007a), as it is the most extensive dataset on the plasma at a comet. As Rosetta was orbiting comet 67P/Churyumov–Gerasimenko (67P) for over 2 yr, the comet's outgassing rate changes significantly as its heliocentric distance varies. An important parameter to classify and understand the size of the environment and the development of a bow shock is therefore the outgassing rate or gas production rate. The gas production rate is derived from measurements of the neutral water density n_n by the Rosetta Orbiter Spectrometer for Ion and Neutral Analysis Cometary Pressure Sensor (H. Balsiger et al. 2007) with the assumption of a spherically expanding coma and photoionization as the only production mechanism. The gas production rate Q at relevant distances for Rosetta can therefore be calculated as (L. Haser 1957):

$$Q = 4\pi u_n r^2 n_n \tag{1}$$

where $u_n = 1\,\mathrm{km\,s^{-1}}$ is an estimate of the neutral expansion velocity and r is the spacecraft's cometocentric distance.

Plasma measurements are made by the Rosetta Plasma Consortium (RPC; C. Carr et al. 2007). The plasma density is available through different derived datasets based on observations by RPC-Langmuir Probe (LAP; A. I. Eriksson et al. 2007) and RPC-Mutual Impedance Probe (MIP; J. G. Trotignon et al. 2007). A detailed description of all available density estimates can be found in the RPC-LAP User Guide.[6] Since the search for jet-like features requires a time resolution of the order of a few seconds, only the MIP-LAP cross-calibrated dataset is suitable, as it provides high absolute accuracy for periods of hours as well as a time resolution of usually 0.017 s. Other density estimates (referred to as N_ED and N_EL in the archive) are included in the figures for background comparison, but their temporal resolution (N_EL) or their absolute accuracy (N_ED) is insufficient for the identification of events. It is assumed that the data quality is good if all estimates agree. For readability, we shall refer to the MIP-LAP cross-calibrated density as the plasma density.

The ion spectra are provided by the Ion Composition Analyser (ICA; H. Nilsson et al. 2007), an ion spectrometer that is capable of distinguishing between the three main ion species: water, hydrogen (protons), and He^{2+}. It takes 192 s to complete a full spectrum with a field of view (FOV) of $90^\circ \times 360^\circ$ and therefore velocities and densities derived from the spectra have a very low temporal resolution. It is possible for visualization to show the spectra integrated only over azimuth. This results in a higher temporal resolution for slices of ion energy spectra as the elevation is stepped through in time. However, this leads to the introduction of FOV effects, as certain ion populations may only be visible at certain elevations. For limited time periods, RPC-ICA also operates in a high time-resolution mode (G. Stenberg Wieser et al. 2017), providing measurements of the cometary ion population from 0.3 to 82 eV $\mathrm{q^{-1}}$ at 4 s resolution. This comes at the expense of FOV, which is limited to a nominal $5\overset{\circ}{.}6 \times 360^\circ$. The ions measured by ICA are heavily influenced by the negative spacecraft potential (S. Bergman et al. 2020). Ions are accelerated into the instrument and can have quite deformed trajectories, obscuring their origin within the measurements. We therefore cannot use the directional information in the high time-resolution mode. To compensate for the additional acceleration of the ions, we trace the lower cutoff of the energy distribution and use this as an estimate for the negative spacecraft potential $-U_{\mathrm{s/c}}$. The corrected energies are then calculated as $E_{\mathrm{corr}} = E_{\mathrm{meas}} - U_{\mathrm{s/c}}$.

The magnetic field was measured by the RPC-Magnetometer (MAG; K.-H. Glassmeier et al. 2007b) at a maximum frequency of 20 Hz. A consistent, long-term dataset exists at a cadence of 1 vector per second. The error of the calibration of this instrument is usually at <3 nT per component, but from 2016 April onward the calibration becomes more uncertain. The direction of the magnetic field is also shown by the clock angle θ and cone angle ϕ. They are defined as follows:

$$\tan\theta = \frac{B_z}{B_y},\ \ \tan\phi = \frac{\sqrt{B_y^2 + B_z^2}}{B_x}. \tag{2}$$

The plasma density was resampled to the same interval as the magnetometer data with 1 s resolution. This is sufficient for the selection algorithm and gives a consistent sampling period for the entire dataset. The trajectory and attitude of the spacecraft were calculated from official SPICE kernels, and all coordinates are in Cometocentric Solar Equatorial coordinates.[7] The x-axis is the comet-Sun line, the z-axis is parallel to the component of the Sun's north pole orthogonal to the x-axis, and the y-axis completes the right-handed reference frame. The comet nucleus' center of mass is the origin of the coordinate system.

2.2. Event Identification

The interval selected for this study is 2015 October 15 to 2016 April 1. As jets are usually associated with the bow shock and are modified as they transition the magnetosheath, intervals where Rosetta is as close to the bow shock as possible are most promising. The spacecraft never crossed the bow shock itself, although there may have been crossings of an early-stage infant bow shock (H. Gunell et al. 2018; C. Goetz et al. 2021). This infant bow shock is highly asymmetric due to ion gyroradius effects, but has a similar effect on the plasma. Due to a lack of direct measurements at 67P, we have to rely on models to infer the bow shock's location.

C. Koenders et al. (2013) presented a model that has been shown to fit most cometary bow shock observations (N. J. T. Edberg et al. 2024). Using the above models, the interval from 2015 October to 2016 March was deemed most promising, as this time period shows the bow shock decreasing in size and approaching the cometocentric distance of Rosetta (Figure 1), before no longer being considered a fully developed bow shock by the model. We define $(\rho u_x)^*_{\mathrm{crit}}$ as 1.3 (N. J. T. Edberg et al. 2024) and assume a photoionization frequency of $7 \times 10^{-7}\,\mathrm{s^{-1}}$ at 1 au, following an inverse square law to the heliocentric distance of the comet. For solar wind parameter inputs, we use the ENLIL model (D. Odstrcil 2003) outputs at the comet. We also use a Haser (Equation (1)) gas production profile that assumes a radially symmetric coma, as this is reasonable for the bow shock calculations in this study.

6 https://archives.esac.esa.int/psa/ftp/pub/mirror/INTERNATIONAL-ROSETTA-MISSION/RPCLAP/RO-SS-RPCLAP-2-RVM1-EDITED2-V1.0/DOCUMENT/RO-IRFU-LAP-UG.PDF

7 https://www.cosmos.esa.int/web/spice/spice-for-rosetta

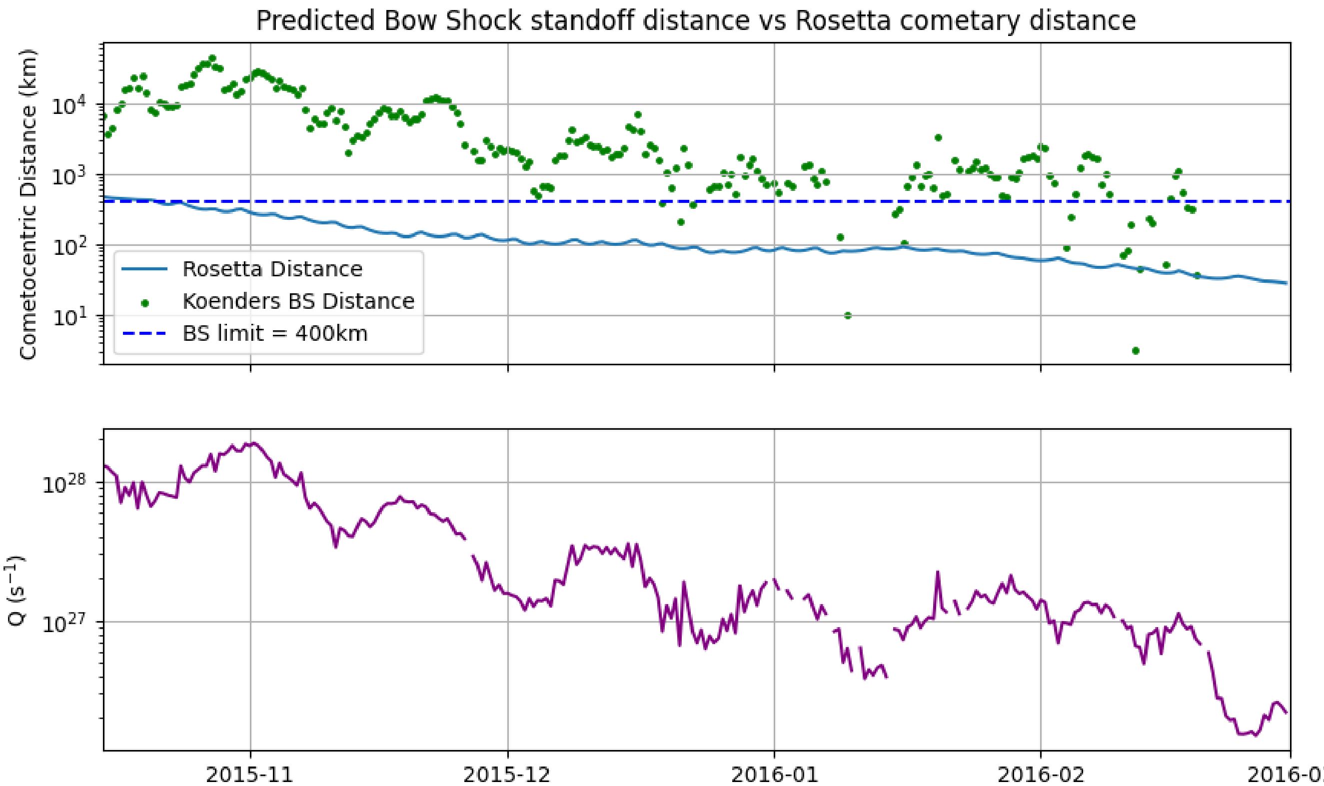

Figure 1. Bow shock standoff distances from 2015 October to 2016 March, calculated with the C. Koenders et al. (2013) model using ENLIL solar wind inputs and a Haser outgassing rate model calculated from measured neutral densities (second panel) as discussed in Section 2.2. The blue dashed line is the theoretical minimum size limit of a fully developed bow shock; at this size, it would instead be considered an infant bow shock (H. Gunell et al. 2018).

As shown in Figure 1, the bow shock size decreases as the outgassing rate decreases; this is due to lower insolation as the comet moves outward in the solar system. The impact of an interplanetary coronal mass ejection in early October is excluded as the plasma was too disturbed to compare to the remainder of the interval (N. J. T. Edberg et al. 2016a).

Jets are defined as short-time enhancements in the dynamic pressure. These enhancements are either defined against a running average of the background dynamic pressure (usually around 10–20 minutes) or against the solar wind measured upstream of the magnetosphere (F. Plaschke et al. 2018a). The available data at comet 67P limit our options to the first method, as solar wind conditions are not measured at the comet (C. Goetz et al. 2022). The Rosetta data also do not include plasma velocities at sufficient time resolution; therefore, we fall back on searching for enhancements in density only, as was done by T. Karlsson et al. (2015) and O. Gutynska et al. (2015), who used density only to identify plasmoids and jets in Cluster data at Earth. M. O. Archer & T. S. Horbury (2013) showed that density-driven jets are common at Earth. T. Mohammed-Amin et al. (2025) have shown that a majority of jets at Mars are density driven, and as Mars is the most suitable analog for a comet, the assumption is that this may also apply to comets (M. Holmstrom & X.-D. Wang 2015). The selection algorithm therefore runs through the following steps:

1. Calculate the average density n_{ave} over a moving 600 s window and calculate the ratio of the plasma density to this background density: $\frac{n}{n_{\text{ave}}}$.
2. Find peaks in $\frac{n}{n_{\text{ave}}}$ that have a minimum height of 2 and a prominence of 0.5. Prominence is defined in the `SciPy` Python package "as the vertical distance between the peak and its lowest contour line,"[8] i.e., the distance to the highest minimum next to the peak.
3. Remove peaks that lie within the steepened wave periods that were identified by K. Ostaszewski et al. (2020).
4. Calculate the magnetic field magnitude average over the same interval as above and calculate $\frac{B}{B_{\text{ave}}}$.

To identify if there are magnetic field peaks or dips associated with the density increase, we check if a value of $\frac{B}{B_{\text{ave}}} > 1.5$ or $\frac{B}{B_{\text{ave}}} < 0.5$ exists within 6 s of the start and end of the density peak. This is not used for the selection algorithm.

The choice of parameters for the selection based on density follows T. Mohammed-Amin et al. (2025). The parameters for the magnetic field peak selection are a trade-off between the number of events and similarity to the density selection. The third step is necessary as steepened waves in the magnetic field are ubiquitous in the environment, and they can be misidentified by this algorithm as jet candidates. However, their features are distinct from jets, as they display a clear asymmetry with a steep increase and a gradual decrease of the magnetic field and density. Steepened waves are also preferentially detected in the magnetic field with limited density signatures (E. Odelstad et al. 2020). Therefore, they are removed from the event set to avoid interference.

[8] https://docs.scipy.org/doc/scipy/reference/generated/scipy.signal.peak_prominences.html

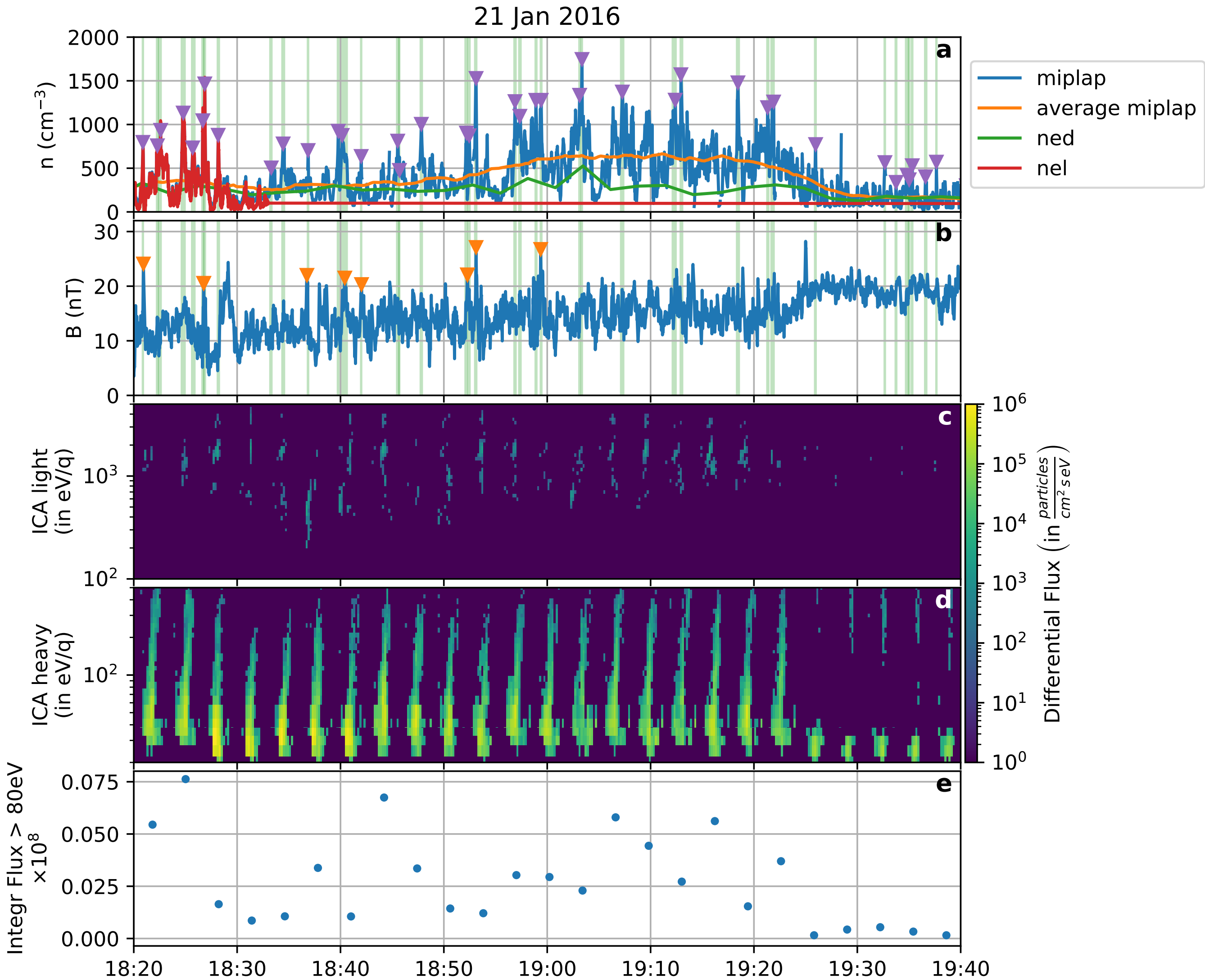

Figure 2. Example interval on 2016 January 21 showing a number of density enhancements. From top to bottom: (a) plasma density from three different estimates with enhancements shaded in green and peak marked by a purple arrow; (b) magnetic field magnitude with density enhancements in green and magnetic field peaks marked in orange; (c) solar wind light ion energy spectrum (not integrated over elevation); (d) cometary heavy ion energy spectrum (not integrated over elevation); (e) integrated flux of cometary ions above 80 eV.

3. Results

3.1. Event Structure

The search algorithm gives a total of 47,063 possible candidates, 5525 of which are associated with peaks or dips in the magnetic field. Figure 2 shows an 80 minute interval on 2016 January 21 with the identified density enhancements marked in the top panel. This interval is typical of many intervals in this study and contains 39 candidates, 10 of which are associated with a peak in the magnetic field. There is no discernible periodicity to the occurrence of events.

The ion energy spectra have not been integrated over elevation to improve time resolution, but this comes at the cost of simplicity. To illustrate, the cometary ion spectra in panel (d) show a distinct shape where a high flux, low-energy population is scanned first before a low-flux, high-energy population comes into the FOV of the instrument. This is expected, as the low- and high-energy ions usually come from different directions (E. Behar et al. 2018; A. Moeslinger et al. 2024). For the first hour of the data, the density (panel (a)) is on average higher and the magnetic field is on average around 15 nT with variations of $\pm$ 10 nT (panel (b)). The solar wind ions (panel (c)) are measured at energies that correspond to a slowed-down, deflected ion trajectory with speeds between 100 and 400 km s^{-1}. Accelerated cometary ions (panel (d)) can reach energies of up to 400 eV q^{-1}, a typical value for that ion population. At the same time, there is also a signature of a newborn ion population, at energies below 80 eV q^{-1}. Panel (e) shows the integrated ion flux for all ions of the accelerated population ($>$ 80 eV q^{-1}), which is elevated in the first hour compared to the last 20 minutes. Around 19:23, the environment changes, resulting in a lower density and a more stable and elevated magnetic field. At the same time, the accelerated and solar wind ions vanish from the measurements, either due to moving out of the FOV or due to a real absence in the plasma. Since the magnetic field changes direction at that time, it is likely that the change in convective electric field direction accompanying the magnetic field change has moved the ions out of the FOV of the instrument. The integrated flux drops to about one-tenth of its initial value. Although the two

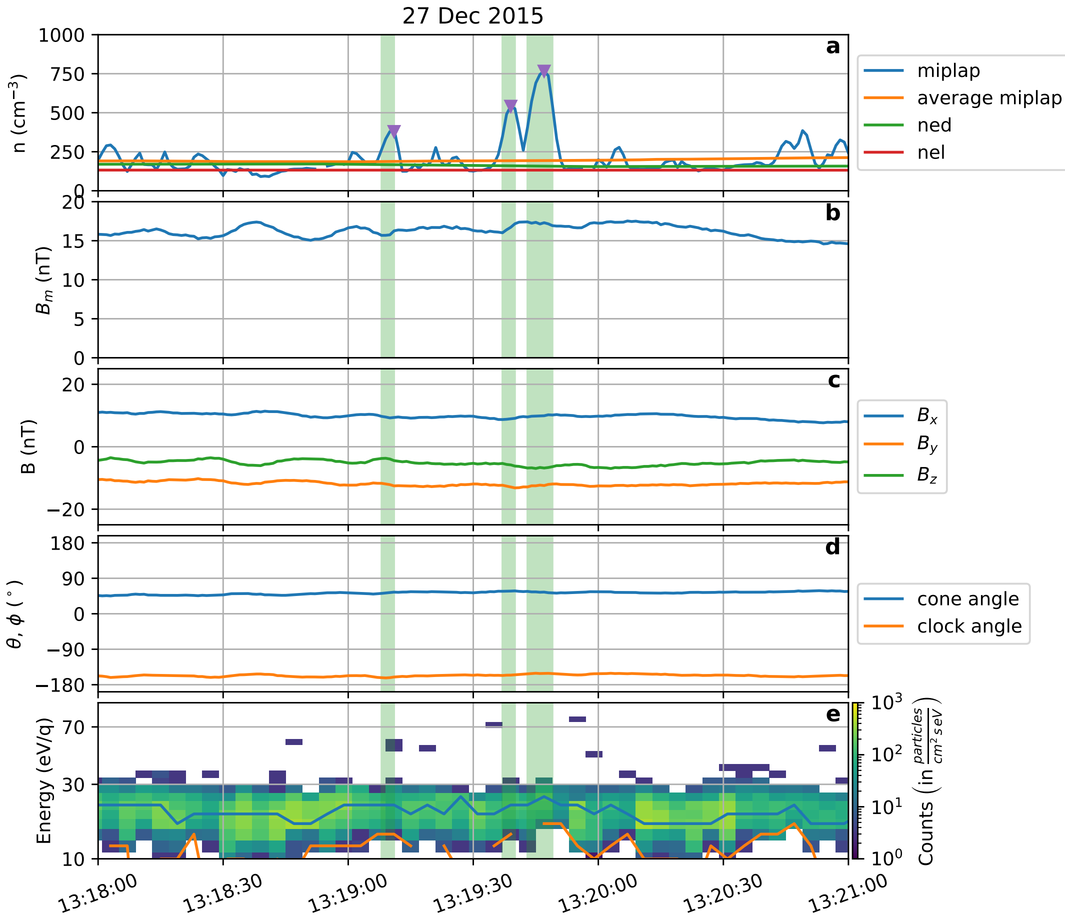

Figure 3. Detailed observations during three density enhancements. (a) plasma density with density enhancement shaded in green and peak indicated by a purple triangle; (b) magnetic field magnitude; (c) magnetic field components; (d) magnetic field cone and clock angle; (e) ICA high-resolution cometary ion spectra with the lower cutoff due to spacecraft potential marked in orange and the peak of the distribution marked in blue.

subintervals are very different, density enhancements are detected throughout the interval.

One might think jet candidates are detected preferentially within the accelerated, anti-sunward ion population, as this population is directly accelerated by momentum and energy exchange with the solar wind, which traverses the bow shock. However, events are also identified when the plasma seems to contain less accelerated ions. This could either be because the instruments are unable to measure the accelerated ions but FOV-independent density features can still be detected, or because these features exist in both the accelerated and radially expanding low-energy ion population.

A close-up of an event is shown in Figure 3. The event is typical of many events identified by the algorithm. There are three very large density enhancements that satisfy the selection criteria, none of which are associated with an increase in magnetic field. Indeed, the field is steady within a few nT, and does not change direction at all. The bottom panel of the figure shows the ICA high time-resolution energy spectra. The blue line traces the peak of the spectrum, and the orange line indicates the inferred spacecraft potential. While all three events are associated with an increase in the peak's energy, they also show a pronounced increase in the spacecraft potential, which is due to the higher density. The corrected energy for these three events is about 2 eV q^{-1} above the ions measured outside for the events. This is within the error bars, and it is therefore not possible to confirm whether the velocity of the ions is indeed elevated. All three events are shorter than 7 s and therefore only cover one ion spectrum even in high-resolution mode. We therefore cannot rule out that there may be a short-lived increase in velocity.

Figure 4 shows a second example of two density increases, one of which is associated with a pronounced peak in the magnetic field magnitude. The magnetic field direction is stable, therefore indicating a purely compressional structure. The second density increase is not associated with a magnetic field change, even though it is similar in magnitude. The ion spectra show a typical enhancement in ion energy for the first event, and less for the second. This could be due to the second event not aligning well with the duration of one ion spectrum.

3.2. Event Statistics

As we have identified over 47,000 events, a statistical analysis of the properties and occurrence of the density increases is possible. Figure 5 shows the occurrence of events throughout the investigated time interval. The top panel shows that events (in purple) are rare before the end of 2015 November, when gas production is relatively high, and the diamagnetic cavity (blue dots) and steepened waves (orange) occur (C. Goetz et al. 2016, 2022; K. Ostaszewski et al. 2020). This is not an effect of data availability, as density data are plentiful within the entire interval (black). Steepened waves are a dominant feature during the first half of the interval and drop off sharply in the second half. Our density features do not

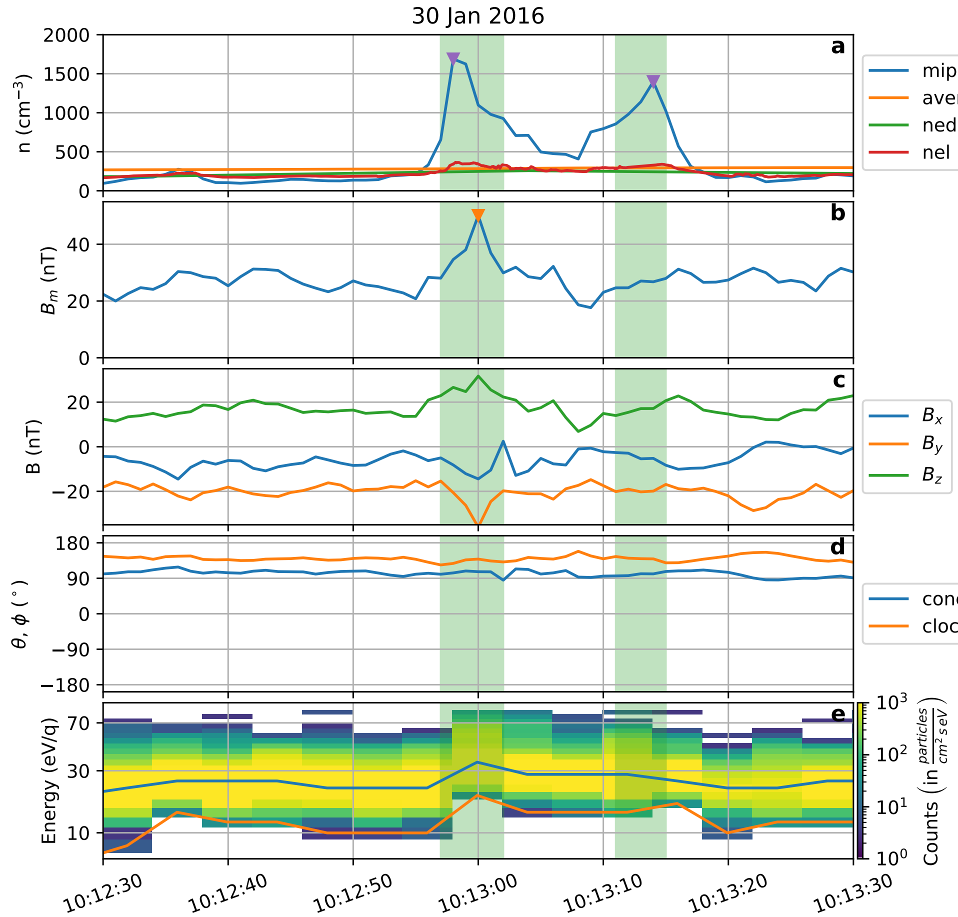

Figure 4. Detailed observations during two density enhancements. (a) plasma density with enhancements shaded in green and peak indicated by a purple triangle; (b) magnetic field magnitude and peak indicated by an orange triangle; (c) magnetic field components; (d) magnetic field cone and clock angle; (e) ICA high-resolution cometary ion spectra with the lower cutoff due to spacecraft potential marked in orange and the peak of the distribution marked in blue.

exhibit the same asymmetry as the steepened waves and are therefore likely unrelated. The density events and the steepened waves seem to simply be features of the coma at different outgassing rates. The diamagnetic cavity ceases to be observable around the same time, with only very few, isolated events in January and February (C. Goetz et al. 2016). Most density events are found between mid-January and mid-February. Panel (b) of Figure 5 shows the occurrence of the density increases in relation to the number of identifiable magnetic field peaks and dips. There seems to be no overall pattern; only in the period from mid-January to mid-February there may be a slight decrease in the occurrence of associated magnetic field structures. This corresponds to the interval with increased density feature detection. Only 12% of all density events are associated with any significant magnetic field structure. Of those, 33% are dips and 67% are peaks. The last panel shows that the integrated accelerated cometary ion flux decreases overall with time, as the gas production rate decreases. This is in accordance with expectations (C. Goetz et al. 2022). Occasional increases in flux are usually due to solar wind events such as coronal mass ejections or corotating interaction regions (N. J. T. Edberg et al. 2016a, 2016b). There is no obvious correlation between the flux of accelerated ions and the occurrence of density increases. Figure 6 shows the occurrence of events, background availability, and the ratio of the two in a two-dimensional space of cometocentric distance of the measurement and gas production rate. Due to spacecraft trajectory constraints, only a limited volume in the space is explored, but within that volume there is good coverage with density measurements. While most events are found at distances <30 km, this is an observational bias, and the ratio clearly shows more detections in the 20–70 km range. Most events are found at gas production rates between 10^{26} and 3×10^{27} s^{-1}. This range exactly corresponds to the increase in events found between mid-January and mid-February. It is not possible to disentangle the spatial from the temporal in these measurements as no repeating orbits were flown.

The investigation of ion velocity measurements at these timescales is challenging, but there are around 7000 events that occur when high-resolution ion data is available. The blue bars in Figure 7 show the corrected (for spacecraft potential effects) energy of the ions during a density increase. The mean energy of this distribution is 12.6 eV which corresponds to an average ion speed of 11.5 km s^{-1}. The purple line shows the corrected energy distribution for the two spectra surrounding each event. The mean energy of this distribution is 11.9 eV or 11.2 km s^{-1}. This is only a minimal increase. We have therefore performed a paired Student's *t*-test to ascertain if the difference between these two distribution functions is statistically significant. We attain a *p*-value of 1.4×10^{-23} for the hypothesis that the energy distribution outside of the events has a smaller mean than that within an event. This is well below the common significance threshold of 0.05 and thus shows that the increase in velocity within the events is statistically significant, if small.

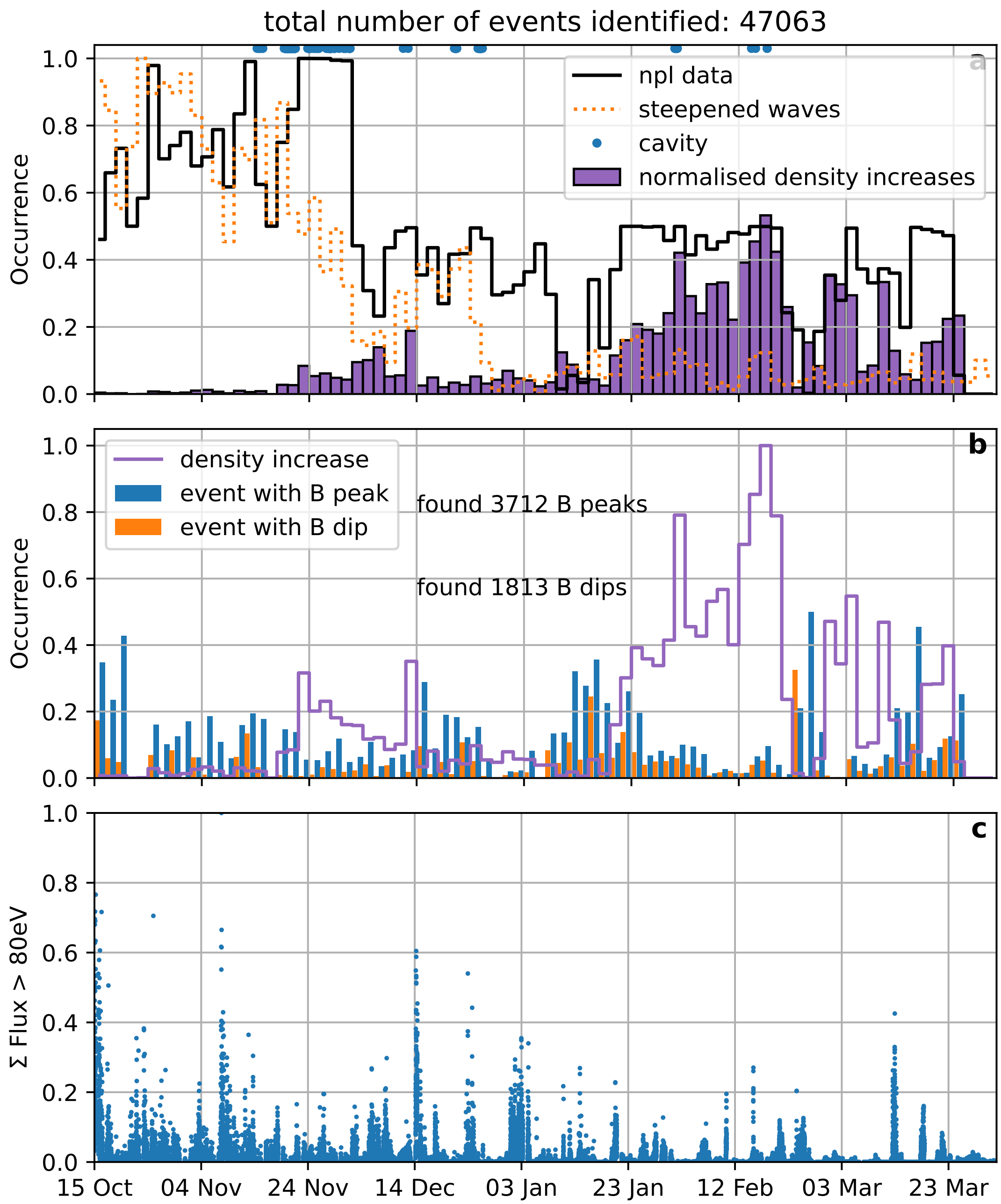

Figure 5. Analysis of density increases. From top to bottom: (a) occurrence of density increases in purple, normalized to the availability of plasma density measurements, availability of plasma density measurements normalized to 1 in black, steepened waves occurrence normalized to one in orange dashed and diamagnetic cavity occurrences as blue dots; (b) occurrence of density increases normalized to 1 in purple with magnetic field peaks and dips in blue and orange; (c) integrated flux of heavy ions above 80 eV. The flux was normalized to one, as only changes are relevant.

Compared to Earth and Mars, these velocities are still quite low, as jets are found at typical velocities of $>300\ \mathrm{km\ s^{-1}}$. However, the ICA high-resolution mode is not able to measure those velocities in any case, as it scans at higher cadence at the expense of the energy range above $82\ \mathrm{eV\ q^{-1}}$. Therefore, we are limited to investigating the velocity of the newborn ion population during these events.

Statistics of the properties of events are shown in Figure 8. The duration of these density increases is similar to those observed at Mars, though slightly shorter (4.3 s instead of 7 s at Mars, T. Mohammed-Amin et al. 2025). At Earth, jet duration varies considerably but tends to be longer than at Mars (F. Plaschke et al. 2018b).

The mean (median) ratio between peak density and background at the comet is 2.9 (2.5), which is very similar to the dynamic pressure increase ratio at Mars (2.3) and only slightly higher than the density increase there (1.9; T. Mohammed-Amin et al. 2025).

On a case-by-case basis, there is no clear relationship between the magnetic field and the density increases, with both dips and peaks being observed during an event. Statistically, however, the background magnetic field is slightly elevated compared to the magnetic field during a density enhancement. This contrasts with jets at Mars, where there is also no clear dependence, but statistically the magnetic field increases during an event (for all values at Mars see T. Mohammed-Amin et al. 2025). This is

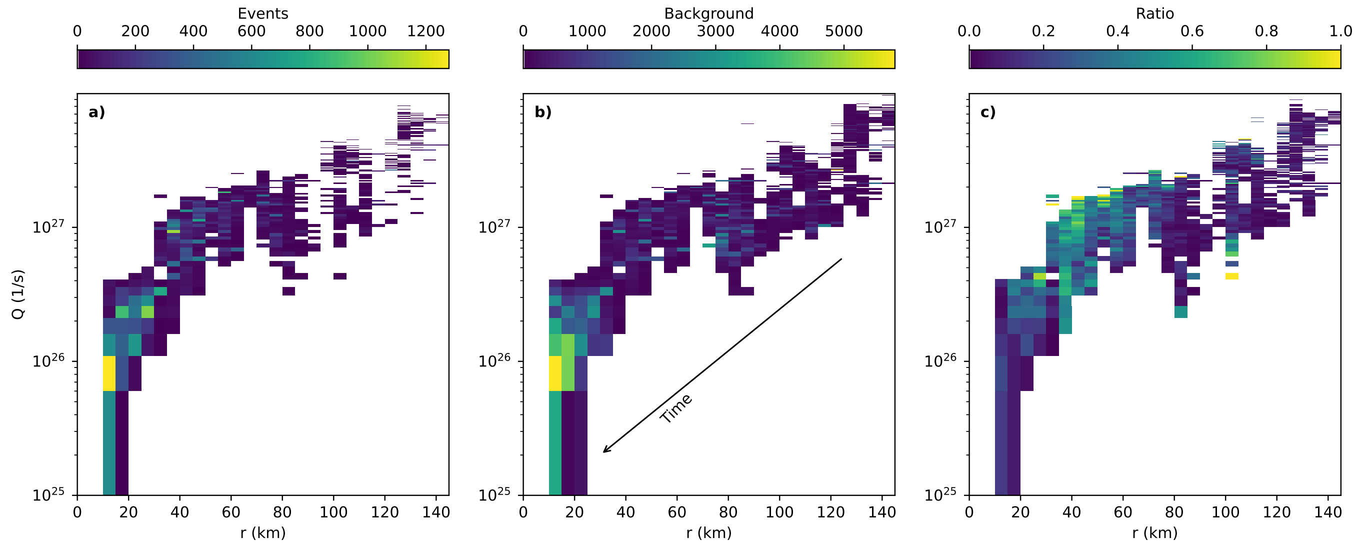

Figure 6. From left to right: histogram of event detections in cometocentric distance–gas production rate space; histogram of the available density measurements in the same axes; and the ratio of detections to measurement availability. The arrow in the middle panel indicates roughly how the spacecraft moves over time in this space: decreasing distance at a steadily decreasing gas production rate.

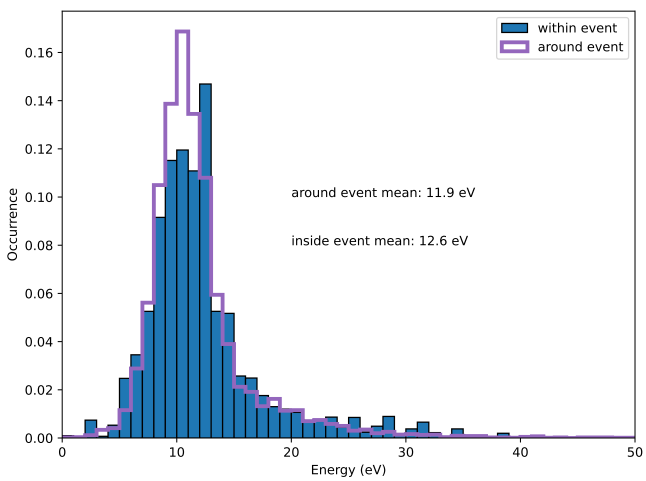

Figure 7. Histogram of average corrected cometary ion energy within the identified density increases, compared to the corrected energy in the two spectra surrounding each of the events.

further reflected in the distribution of $B/B_{\rm ave}$ in panel (d), which is symmetric about 1, with a mean and median of 1.07 and 1.03, respectively, indicating that on average there is no difference in magnetic field within the event compared to the average.

At Earth, jets occur preferentially downstream of the quasi-parallel bow shock. For the events presented here, it is not possible to determine whether they are associated with the quasi-parallel bow shock at the comet, as Rosetta does not measure the undisturbed solar wind and the draping of the magnetic field precludes an inference of which hemisphere contains the quasi-parallel bow shock. We are therefore unable to study a potential link to the quasi-parallel bow shock at 67P.

A direct comparison of occurrence rates between the comet and those reported at Earth or Mars is complicated by the very different spacecraft trajectories involved. While planetary missions follow well-defined periodic orbits, the trajectory of the Rosetta spacecraft is (1) mostly not circular or elliptical and (2) covers very little radial distance within timescales of weeks. The highest occurrence rate is 1644 events per day or 68.5 events per hour on average on 2016 February 16. This is significantly higher than what is found at Mars (up to approximately six events per hour, T. Mohammed-Amin et al. 2025). A comparison to rates measured at Earth is difficult, as values vary significantly depending on jet size and location within the magnetosheath. L. Vuorinen et al. (2019) present a comprehensive investigation of occurrence rates under different IMF conditions and at different locations within the magnetosheath. The occurrence rates vary between a few jets per day and up to almost 200 small jets per hour (Figure 5 in L. Vuorinen et al. 2019). Our study is not able to distinguish between location and IMF conditions, so we cannot make a detailed comparison, but the occurrence rates at the comet seem to be at least within the bounds established at Earth.

4. Discussion and Conclusion

We have identified a large number of density enhancements at comet 67P, which share many characteristics with magnetosheath jets at Earth and Mars. Between 2015 October and 2016 March, we found 47,063 events, 12% of which are associated with either peaks or dips in the magnetic field. Most events are identified between mid-January of 2015 and mid-February of 2016, which corresponds to a gas production rate of 10^{26} and 3×10^{27} s^{-1} and a rough cometocentric distance of 20 to 70 km. This means that events are found inside and outside of the solar wind ion cavity, and we do not find any correlation between the occurrence of events and the energy of the accelerated cometary ion population.

Some density increases also show an increase in the velocity of heavy ions, but the data are very difficult to interpret due to limited energy coverage and time resolution. However, a paired *t*-test confirms that on average the velocity of the newborn cometary ion population is elevated from 11.2 to 11.5 km s^{-1}. This is a very small increase only, but data for the accelerated cometary ions and the solar wind are not available; thus, they could exhibit a larger increase. It is possible that what we observe are signatures of magnetosheath jets that have transferred from the solar wind and accelerated ion population into the cometary ion population. The density

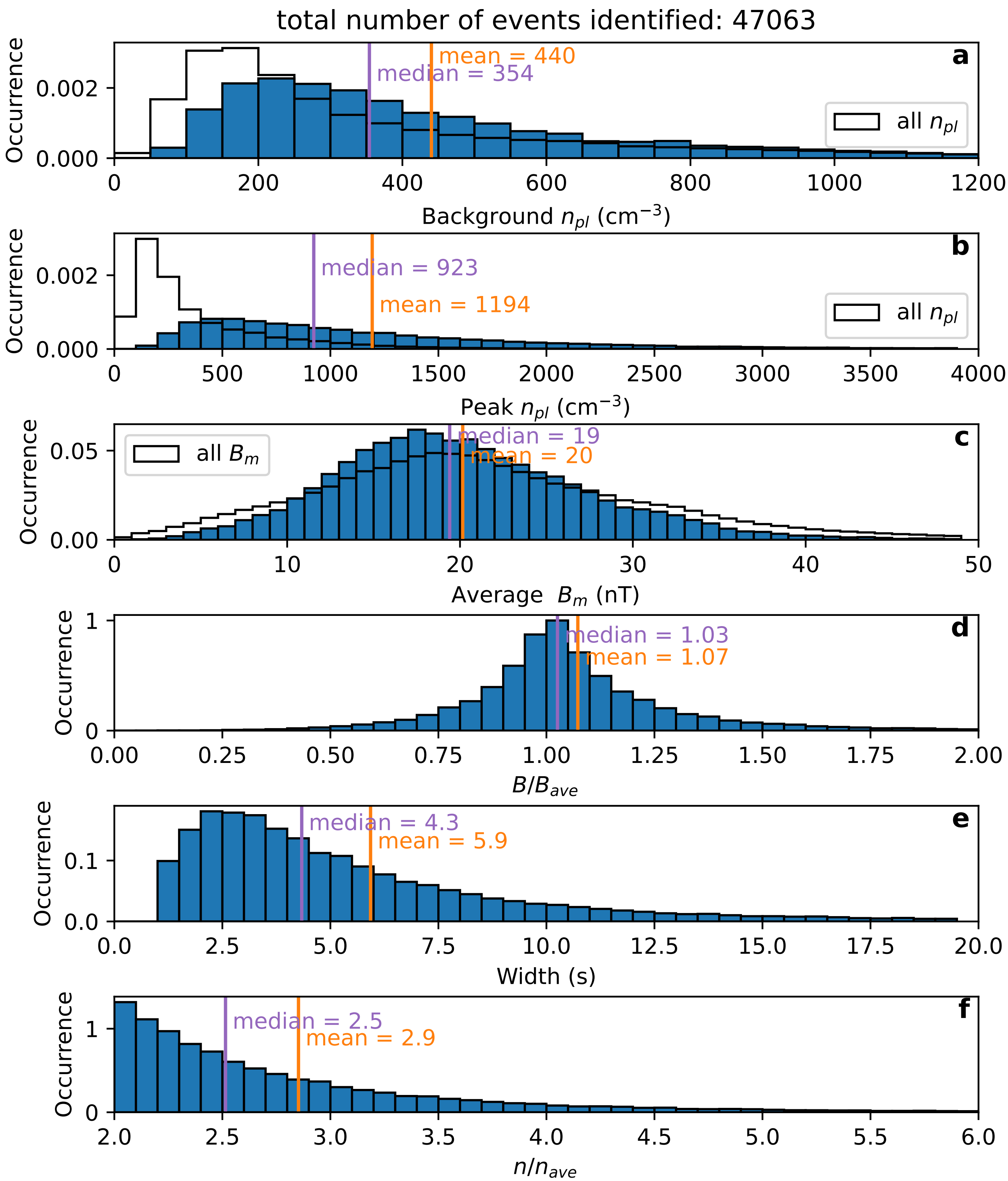

Figure 8. Characteristics of events compared to the entire study interval. From top to bottom: (a) background plasma density within the density increase (blue) and for the whole interval (black); (b) peak density of the increase compared to the density of the whole study interval; (c) magnetic field magnitude within the density enhancement and the entire study interval; (d) magnetic field magnitude during the event divided by the 300 s average; (e) occurrence of width of candidate in seconds; (f) occurrence of height of peak above average. The median and mean are with respect to the event distribution, not the background.

measured during the increase is likely a combination of an increase in the accelerated and newborn cometary ion population.

There is no pattern to the occurrence of magnetic field dips or peaks associated with density increases, and at least on a timescale of a few minutes, a magnetic field change does not change the occurrence rate of events. A possible explanation is that the density is dominated by slow ions, which may be largely decoupled from the magnetic field due to their large gyroradii, with the field instead carried by the electrons.

This decoupling also implies that the magnetic field alone cannot be used to identify jet-like structures at comets, since most events are not associated with a magnetic field feature. These structures are not embedded in the solar wind ions or accelerated cometary ions directly, implying that they have undergone some modification as they travel through the plasma and transfer from one population to another. This is similar to magnetic holes, which have been shown to traverse the environment with only minor modifications (F. Plaschke et al. 2018b).

We find that the duration of events is only slightly shorter than at Mars and shorter than at Earth. Y. Zhou et al. (2024) hypothesized that jet duration scales inversely with bow shock standoff distance; since the bow shock at 67P is estimated to be quite small at the time that these density enhancements are identified, our findings are consistent with that hypothesis.

The peak density to background density ratio is similar to what is found at Mars, but the occurrence rate is much higher than at Mars. T. Mohammed-Amin et al. (2025) hypothesize that the increase in wave activity in the Martian foreshock compared to Earth makes Martian jets less dependent on being created at the quasi-parallel bow shock. The wave activity in the foreshock region of a comet should be even more enhanced due to the large density of pickup ions. This could explain the much higher occurrence rates at 67P. It is also possible that the trajectory of the spacecraft contributes to higher rates, as the spacecraft does not traverse different regions.

The structures occur during intervals identified as being as close to the bow shock as possible with Rosetta's trajectory, and they appear as steepened waves cease to be detected. This indicates that the density enhancements are a feature of the inner coma at the intermediate-activity stage, in contrast to, e.g., steepened waves and the diamagnetic cavity, which are a feature of the inner coma at high activity. We would also expect the density enhancements to exist at higher activity stages, but due to the larger size of the interaction region and the spacecraft trajectory (inner coma only at high activity), it is not possible to observe them. However, it is not possible to unambiguously establish that these structures are created at the bow shock and are convected with the flow toward the comet. Local generation cannot be excluded, but no mechanism is known to cause such density increases in the inner coma. The lack of magnetic field signature associated with 88% of density increases also indicates that these events are unlikely to be mirror modes, magnetic holes, or magnetosonic waves, as all of those are associated with clear magnetic field features. If we assume that all 12% of magnetic field feature events are magnetic structures like mirror modes, magnetic holes, or magnetosonic waves, we should remove all events with clear magnetic field features. However, this does not change any of the statistical properties significantly. We therefore conclude that the density increases found by our method are independent structures and not manifestations of known magnetic field features.

To conclude, these structures may potentially be classified as magnetosheath jets. However, definitive velocity-based classification is not possible due to insufficient temporal and energy resolution in the available measurements. The events found and presented in this paper could be related to cometosheath jets: the structures reside within the cometosheath and exhibit a localized dynamic pressure increase which shares characteristics with magnetosheath jets at Mars. Notably, the observed density enhancements are found in the cometary ion population, which distinguishes these cometary structures from analogous jets reported at Mars and Earth and implies that cometosheath structures could be a direct result of solar wind structures upstream of the inner coma. However, the generation mechanism of these structures remains ambiguous; without knowledge of their spatial origin and the exact bow shock location and upstream magnetic field, it is not possible to determine whether they arise from foreshock-associated wave activity upstream of the bow shock or are generated locally within the cometosheath. We are not aware of any mechanisms that could cause such structures at that cometary activity stage. Without additional data, it will not be possible to investigate the origin further, but the three-point measurements that are anticipated during the Comet Interceptor mission due to launch in 2029 may give more clarity in the future. It may also be possible to confirm the existence of jets in future simulations of the plasma environment at comets.

Acknowledgments

We acknowledge the invaluable discussions at the ISSI team 24-627 on "Magnetosheath structures as seen by spacecraft observations and numerical simulations." C.G. is supported by a UKRI Future Leaders Fellowship (UKRI2308: COMMIT). R.D.M. is supported by an ESA OSIP co-sponsored PhD studentship. C.G. and R.D.M. acknowledge invaluable technical support provided by Alexander D. Tempest. H.G. and A.M. are supported by the Swedish National Space Agency, contract 2023-00208. C.S.W. was supported by the Austrian Science Fund (FWF) 10.55776/P35954. E.K. was supported by Vetenskapsrådet grant 2018-03623 and the Swedish National Space Agency under grant 2022-00138.

Author Contributions

C.G. conceptualized the project, performed the data analysis, and wrote the first draft. R.D.M. performed a pilot study and the bow shock distance calculations. All authors contributed to discussion and interpretation of the results.

Appendix A
Impact of Steepened Wave Removal on Event Distribution

To ensure that the removal of the steepened waves does not significantly impact the distribution of events, we have calculated the percentage of events removed for each day in the study interval. Figure 9 shows the number of events identified before steepened wave removal and the number of events removed (upper panel). The lower panel shows the percentage of removed steepened waves.

While the percentage is high at the beginning of the interval (∼50%), the overall number of events identified before removal is very low already and therefore a disproportionate number of events is removed. Once more events are identified from mid-November onwards, the percentage decreases significantly (20% at most). We therefore conclude that the steepened wave removal has no significant impact on the analysis.

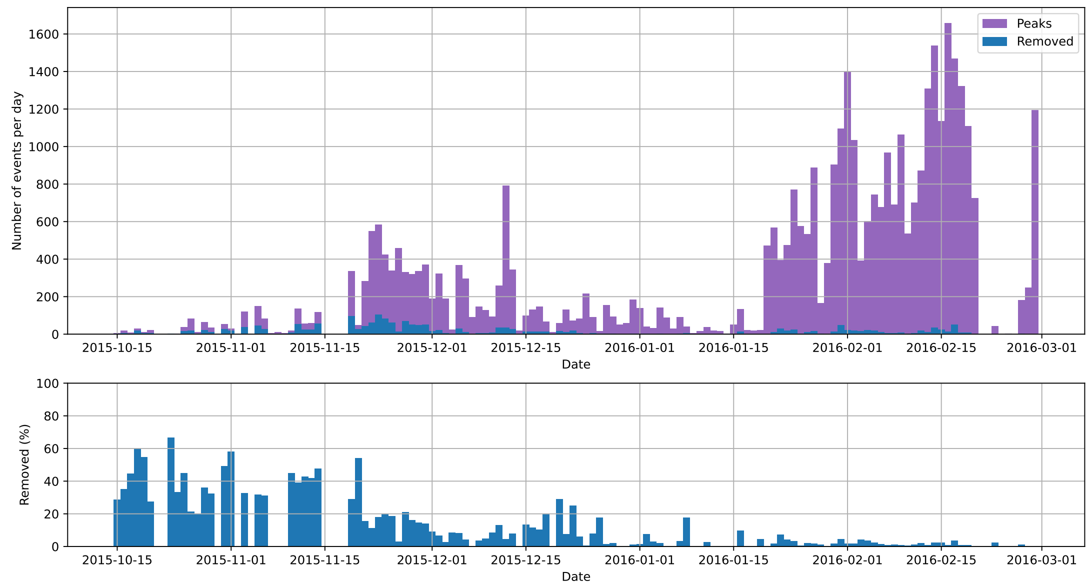

Figure 9. Top: number of peaks identified and number of peaks removed due to steepened waves. Bottom: percentage of events removed due to steepened waves.

Appendix B
Software and Third Party Data Repository Citations

The datasets created in this work (event list and background value calculations) can be found at doi:10.5281/zenodo.19706194. The Python code used to analyze the data and produce the figures can be found at https://github.com/ChaGoetz/densityIncreasesComets2026.

ORCID iDs

Charlotte Goetz https://orcid.org/0000-0003-4468-0338
Ruben Doyle-Morgan https://orcid.org/0009-0002-8346-7265
Herbert Gunell https://orcid.org/0000-0001-5379-1158
Eva Krämer https://orcid.org/0000-0002-1826-3613
Tomas Karlsson https://orcid.org/0000-0002-4546-5050
Anja Möslinger https://orcid.org/0000-0003-0587-9598
Cyril Simon-Wedlund https://orcid.org/0000-0003-2201-7615
Martin Volwerk https://orcid.org/0000-0002-4455-3403

References

Archer, M. O., & Horbury, T. S. 2013, AnGeo, 31, 319
Archer, M. O., Horbury, T. S., & Eastwood, J. P. 2012, JGRA, 117, A05228
Balsiger, H., Altwegg, K., Bochsler, P., et al. 2007, SSRv, 128, 745
Behar, E., Nilsson, H., Alho, M., Goetz, C., & Tsurutani, B. 2017, MNRAS, 469, S396
Behar, E., Tabone, B., Saillenfest, M., et al. 2018, A&A, 620, A35
Bergman, S., Stenberg Wieser, G., Wieser, M., Johansson, F. L., & Eriksson, A. 2020, JGRA, 125, e27478
Carr, C., Cupido, E., Lee, C. G. Y., et al. 2007, SSRv, 128, 629
Edberg, N. J. T., Alho, M., André, M., et al. 2016a, MNRAS, 462, S45
Edberg, N. J. T., Eriksson, A. I., Odelstad, E., et al. 2016b, JGRA, 121, 949
Edberg, N. J. T., Eriksson, A. I., Vigren, E., et al. 2024, A&A, 682, A51
Eriksson, A. I., Boström, R., Gill, R., et al. 2007, SSRv, 128, 729
Glassmeier, K.-H., Boehnhardt, H., Koschny, D., Kührt, E., & Richter, I. 2007a, SSRv, 128, 1
Glassmeier, K.-H., Richter, I., Diedrich, A., et al. 2007b, SSRv, 128, 649
Goetz, C., Behar, E., Beth, A., et al. 2022, SSRv, 218, 65
Goetz, C., Gunell, H., Johansson, F., et al. 2021, AnGeo, 39, 379
Goetz, C., Koenders, C., Hansen, K. C., et al. 2016, MNRAS, 462, S459
Gunell, H., Goetz, C., Simon Wedlund, C., et al. 2018, A&A, 619, L2
Gunell, H., Hamrin, M., Nesbit-Östman, S., Krämer, E., & Nilsson, H. 2023, SciA, 9, eadg5703
Guo, J., Lu, S., Lu, Q., et al. 2025, ApJL, 978, L9
Guo, J., Lu, S., Lu, Q., et al. 2026, GeoRL, 53, e2025GL121533
Gutynska, O., Sibeck, D. G., & Omidi, N. 2015, JGRA, 120, 7687
Haser, L. 1957, BSRSL, 43, 740
Hietala, H., Laitinen, T. V., Andréeová, K., et al. 2009, PhRvL, 103, 245001
Holmstrom, M., & Wang, X.-D. 2015, P&SS, 119, 43
Karlsson, T., Kullen, A., Liljeblad, E., et al. 2015, JGRA, 120, 7390
Karlsson, T., Liljeblad, E., Kullen, A., et al. 2016, P&SS, 129, 61
Koenders, C., Glassmeier, K.-H., Richter, I., Motschmann, U., & Rubin, M. 2013, P&SS, 87, 85
Krämer, E., Koller, F., Suni, J., et al. 2025, SSRv, 221, 4
Läuter, M., Kramer, T., Rubin, M., & Altwegg, K. 2020, MNRAS, 498, 3995
Moeslinger, A., Gunell, H., Nilsson, H., Fatemi, S., & Stenberg Wieser, G. 2024, JGRA, 129, e2024JA032757
Mohammed-Amin, T., Krämer, E., Nesbit-Östman, S., Gunell, H., & Simon Wedlund, C. 2025, A&A, 696, A75
Neubauer, F. M., Glassmeier, K. H., Acuña, M. H., et al. 1990, AnGeo, 8, 463
Nilsson, H., Lundin, R., Lundin, K., et al. 2007, SSRv, 128, 671
Němeček, Z., Šafránková, J., Přech, L., et al. 1998, GeoRL, 25, 1273
Nykyri, K., Bengtson, M., Angelopoulos, V., Nishimura, Y., & Wing, S. 2019, JGRA, 124, 4314
Němeček, Z., Šafránková, J., Grygorov, K., et al. 2023, GeoRL, 50, e2023GL106131
Odelstad, E., Eriksson, A. I., André, M., et al. 2020, JGRA, 125, e28592
Odstrcil, D. 2003, AdSpR, 32, 497
Ostaszewski, K., Glassmeier, K.-H., Goetz, C., et al. 2020, AnGeo, 39, 721
Plaschke, F., Hietala, H., & Angelopoulos, V. 2013, AnGeo, 31, 1877
Plaschke, F., Hietala, H., Archer, M., et al. 2018a, SSRv, 214, 81
Plaschke, F., Hietala, H., & Vörös, Z. 2020, JGRA, 125, e27962
Plaschke, F., Jernej, M., Hietala, H., & Vuorinen, L. 2020, AnGeo, 38, 287
Plaschke, F., Karlsson, T., Götz, C., et al. 2018b, A&A, 618, A114
Raptis, S., Karlsson, T., Plaschke, F., Kullen, A., & Lindqvist, P.-A. 2020, JGRA, 125, e27754
Raptis, S., Karlsson, T., Vaivads, A., et al. 2022, GeoRL, 49, e2022GL100678
Stenberg Wieser, G., Odelstad, E., Wieser, M., et al. 2017, MNRAS, 469, S522
Suni, J., Palmroth, M., Turc, L., et al. 2025, JGRA, 130, e2025JA033995
Suni, J., Palmroth, M., Turc, L., et al. 2021, GeoRL, 48, e95655
Trotignon, J. G., Michau, J. L., Lagoutte, D., et al. 2007, SSRv, 128, 713
Vuorinen, L., Hietala, H., & Plaschke, F. 2019, AnGeo, 37, 689
Wang, B., Nishimura, Y., Hietala, H., et al. 2018, JGRA, 123, 4879
Williamson, H. N., Nilsson, H., Stenberg Wieser, G., et al. 2020, GeoRL, 47, e88666
Zhou, Y., Raptis, S., Wang, S., et al. 2024, NatCo, 15, 4